CHEOPS geometric albedo of the hot Jupiter HD 209458 b

Brandeker, A.; Heng, K.; Lendl, M.; Patel, J.A.; Morris, B.M.; Broeg, C.; ... ; Wolter, D.

CHEOPS geometric albedo of the hot Jupiter HD 209458 b[⋆]

A. Brandeker[1][⋆⋆], K. Heng[2,3], M. Lendl[4], J. A. Patel[1], B. M. Morris[2], C. Broeg[2,5], P. Guterman[6,7], M. Beck[4], P. F. L. Maxted[8], O. Demangeon[9,10], L. Delrez[11,12], B.-O. Demory[2], D. Kitzmann[2], N. C. Santos[9,10], V. Singh[13], Y. Alibert[5], R. Alonso[14,15], G. Anglada[16,17], T. Bárczy[18], D. Barrado y Navascues[19], S. C. C. Barros[9,10], W. Baumjohann[20], T. Beck[5], W. Benz[2,5], N. Billot[4], X. Bonfils[21], G. Bruno[5], J. Cabrera[22], S. Charnoz[23], A. Collier Cameron[24], C. Corral van Damme[25], Sz. Csizmadia[22], M. B. Davies[26], M. Deleuil[6], A. Deline[4], D. Ehrenreich[4], A. Erikson[22], J. Farinato[13], A. Fortier[2,5], L. Fossati[20], M. Fridlund[27,28], D. Gandolfi[29], M. Gillon[11], M. Güdel[30], S. Hoyer[6], K. G. Isaak[31], L. Kiss[32,33], J. Laskar[34], A. Lecavelier des Etangs[35], C. Lovis[4], A. Luntzer[36], D. Magrin[13], V. Nascimbeni[13], G. Olofsson[1], R. Ottensamer[36], I. Pagano[37], E. Pallé[14], G. Peter[38], G. Piotto[13,39], D. Pollacco[3], D. Queloz[40,41], R. Ragazzoni[13,39], N. Rando[25], H. Rauer[22,42,43], I. Ribas[16,17], G. Scandariato[37], D. Ségransan[4], A. E. Simon[5], A. M. S. Smith[22], S. G. Sousa[9], M. Steller[20], Gy. M. Szabó[44,45,46], N. Thomas[5], S. Udry[4], V. Van Grootel[12], N. Walton[47], and D. Wolter[22]

(Affiliations can be found after the references)

ABSTRACT

We report the detection of the secondary eclipse of the hot Jupiter HD 209458 b in optical/visible light using the CHEOPS space telescope. Our measurement of $20.4^{+3.2}_{-3.3}$ parts per million translates into a geometric albedo of $A_g = 0.096 \pm 0.016$. The previously estimated dayside temperature of about 1500 K implies that our geometric albedo measurement consists predominantly of reflected starlight and is largely uncontaminated by thermal emission. This makes the present result one of the most robust measurements of A_g for any exoplanet. Our calculations of the bandpass-integrated geometric albedo demonstrate that the measured value of A_g is consistent with a cloud-free atmosphere, where starlight is reflected via Rayleigh scattering by hydrogen molecules, and the water and sodium abundances are consistent with stellar metallicity. We predict that the bandpass-integrated TESS geometric albedo is too faint to detect and that a phase curve of HD 209458 b observed by CHEOPS would have a distinct shape associated with Rayleigh scattering if the atmosphere is indeed cloud free.

Key words. techniques: photometric – planetary systems – planets and satellites: atmospheres – planets and satellites: individual: HD 209458 b

1. Introduction

The albedo of an exoplanet determines how much starlight enters its atmosphere and hence its global energy budget. Measurements of the secondary eclipse (occultation) depth of a transiting exoplanet directly yield the albedo at full phase (Seager 2010), which is known as the geometric albedo (Russell 1916), if only reflected starlight is measured (Heng & Demory 2013) or if thermal emission is accounted for using complementary infrared data (Wong et al. 2020, 2021). Such measurements have been made using the Kepler (Heng & Demory 2013; Angerhausen et al. 2015; Esteves et al. 2015), TESS (Wong et al. 2020, 2021), Hubble (Swain et al. 2009; Beatty et al. 2017; Evans et al. 2013), and CHEOPS (Lendl et al. 2020; Hooton et al. 2021) space telescopes. The most convincing measurement of the geometric albedo of an exoplanet is that of the hot Jupiter Kepler-7b using four years of Kepler data (Kipping & Bakos 2011; Demory et al. 2011, 2013; Angerhausen et al. 2015), although its exact value has been debated in the literature (Esteves et al. 2015; Heng et al. 2021).

HD 209458 b has been and remains one of the most frequently studied hot Jupiters in history since its discovery in 1999 (Henry et al. 2000; Charbonneau et al. 2000). Its Spitzer 4.5 μm phase curve reveals a dayside brightness temperature of about 1500 K (Zellem et al. 2014; Evans et al. 2015). Its optical/visible transmission spectrum, measured by the STIS instrument on board the Hubble Space Telescope (HST), indicates a spectral slope at wavelengths ≲ 600 nm due to Rayleigh scattering (Lecavelier Des Etangs et al. 2008; Sing et al. 2016). Its dayside emission spectrum suggests a water abundance consistent with stellar metallicity and a cloud-free atmosphere at the wavelengths probed by HST-WFC3 (Line et al. 2016). Observations of Fe+ and Mg (Cubillos et al. 2020) might suggest clouds along the terminator (Gao et al. 2020), which would contradict observations of HST-WFC3 versus J bands in transmission that indicate a cloud-free terminator (Stevenson 2016). A potential source of opacity in a cloud-free atmosphere is neutral sodium through its strong resonance lines, whose line wings dominate over a very broad spectral range (Sudarsky et al. 2000). Na has been observed in transmission (Charbonneau et al. 2002; Sing et al. 2008; Snellen et al. 2008; Jensen et al. 2011), although these results have recently been suggested to be analysis artefacts (Casasayas-Barris et al. 2020, 2021). Na and/or TiO in the atmosphere are found to explain the broadband transmission spectrum of the planet best (Santos et al. 2020). Na has never been observed in emission for HD 209458 b (D.K. Sing, 2021,

---

private communication). Other elements of interest are atomic hydrogen, oxygen, and carbon, which have been reported in the extended escaping atmosphere of the planet (Vidal-Madjar et al. 2003, 2004).

Previous efforts to detect the optical/visible occultation of HD 209458 b using the MOST space telescope yielded upper limits ($A_g < 0.17$ [3σ] in the MOST bandpass, Rowe et al. 2006, 2008). In this Letter, we report a robust $> 6\sigma$ detection of the occultation depth of HD 209458 b using the CHEOPS space telescope (Benz et al. 2021) and demonstrate that the corresponding geometric albedo is consistent with a cloud-free atmosphere of a chemical abundance similar to that of the star.

2. Methods

2.1. Observations and data processing

We observed ten occultations of HD 209458 b between July and September 2021 (CHEOPS programme CH_PR100016; see observation log in Table 1). Each visit lasted for about 11 h, corresponding to seven CHEOPS orbits with an efficiency (fraction of time on target) of ~70%. To save bandwidth, groups of three 11.5 s exposures of a circular subarray with a radius of 100 pixels were co-added prior to downlink, resulting in a cadence of 34.5 s. In addition, single-exposure circular imagettes with a radius of 30 pixels were downloaded. We analysed the subarrays using photometry from the *Data Reduction Pipeline* (DRP; Hoyer et al. 2020) and the point-spread function photometry package PIPE[1] developed specifically for CHEOPS (Brandeker et al. in prep.; see also descriptions in Szabó et al. 2021 and Morris et al. 2021) as well as imagette photometry with PIPE. We found that the results were consistent with a ~100 ppm in standard deviation over 1 min bins (for this G = 7.5 mag star), but the imagette photometry resulted in a scatter lower by 10% in the measured occultation depths. This is likely due to the faster cadence of the imagettes, which allows detrending with a higher time-resolution. We thus here focus on the analysis of the imagette photometry.

The light curves were analysed using the pycheops software, a Python module specifically developed to analyse light curves from CHEOPS (Maxted et al. 2021). Data points marked as poor by PIPE (due to e.g. strong cosmic rays or contamination from a satellite passing through the field of view; this affects 527 out of 25 866, i.e., 2.0% of the data points) were masked from the analysis. We also removed data with a background higher than 300 e⁻ pix⁻¹ (an additional 652 out of 25 866, i.e., 2.5%) because they are empirically difficult to reduce adequately, possibly due to non-linear sensitivity linked to charged-transfer inefficiency. The poor data points were flagged at the data reduction stage, uninformed by the extracted light curve. The end result are therefore not biased by the filtering. Each visit was analysed individually, for which we fixed the transit depth and used informative priors based on their literature values given to the transit width, impact parameter, and transit central time (Table A.1). The orbit was assumed to be circular (Deming et al. 2005; Crossfield et al. 2012), such that the occultation time is shifted by half an orbit compared to the transit, corrected for light-travel time. The occultation depth was generally given a broad uniform prior (1–200 ppm), with the exception for visit 5, where the Monte Carlo Markov chain (MCMC) analysis did not converge (using 10^3–10^4 steps and 128–512 walkers). Instead, the occultation depth for visit 5 was derived with an unconstraining improper prior $\mathcal{U}(-\infty, \infty)$, resulting in a negative occultation depth (Table 2). It

is statistically expected for single visits that a negative occultation depth may be derived because the signal-to-noise ratio per visit is low. An initial fit of individual visits was made using the least-square minimisation Python package lmfit, which includes roll angle and (x, y)-position decorrelation (selected so that it results in a Bayes factor < 1). The residuals were then fitted by a Gaussian process (GP), which give strong priors on the GP (based on a preliminary fit in which only GP parameters were free) and the planetary parameters (from the lmfit analysis) for the subsequent GP fit. In the end, all of these visits were analysed simultaneously using the MCMC scheme with the MultiVisit method within pycheops, in which the priors were inferred from the fit to the individual visits. To search for remaining correlations in the residuals, we used the Shapiro-Wilk test (Shapiro & Wilk 1965). The resulting p-value of 0.72 indicates that the residuals are indistinguishable from white noise.

To convert the measured occultation depth into a geometric albedo, we first estimated the contribution from thermal emission by extrapolating the daytime temperature as found by *Spitzer* 4.5 μm occultation measurements (Zellem et al. 2014) to the CHEOPS bandpass assuming an irradiated model atmosphere from Mollière et al. (2015) with the parameters $T_{\rm eff}$ = 1500 K, [Fe/H] = 0.0, C/O = 0.55, irradiating spectral type F5, and log g = 3.0. We then computed the geometric albedo as $A_g = (a/R_p)^2 L$, where L is the occultation depth corrected for thermal emission, and the ratio a/R_p was computed from $a/R_\star$ and $R_p/R_\star$ found in Table A.1.

We estimated the TESS expected detection threshold for the HD 209458 b occultation depth by assuming the sensitivity to be equivalent to existing TESS observations of the similar system HD 189733 b in sector 41. We also computed the thermal contribution in the TESS and MOST bands using the same model atmosphere as before.

2.2. Calculations of geometric albedos

The monochromatic geometric albedo associated with Rayleigh scattering is (Heng et al. 2021)

$$A_{g,\lambda} = \frac{\omega}{16} + \frac{\epsilon}{2} + \frac{\epsilon^2}{6} + \frac{\epsilon^3}{24}, \tag{1}$$

where ω is the single-scattering albedo, $\epsilon = (1 - \gamma)/(1 + \gamma)$ is the bihemispherical reflectance (Hapke 1981), and $\gamma = \sqrt{1 - \omega}$. In the preceding expression, the first term accounts for single scattering of starlight, while the other terms account for multiple scattering. The single-scattering albedo is given by the ratio of cross sections,

$$\omega = \frac{0.9\sigma_{\rm H_2}}{0.9\sigma_{\rm H_2} + \sigma_{\rm abs}}, \tag{2}$$

where the Rayleigh scattering cross section due to molecular hydrogen is (Cox 2000)

$$\sigma_{\rm H_2} = \frac{24\pi^3}{n_{\rm ref}^2 \lambda^4} \left(\frac{k^2 - 1}{k^2 + 2}\right)^2, \tag{3}$$

$n_{\rm ref} = 2.68678 \times 10^{19}$ cm⁻³, λ is the wavelength, and the refractive index is

$$k = 1.358 \times 10^{-4} \left[1 + 0.00752 \left(\frac{\lambda}{1\,\mu{\rm m}}\right)^{-2}\right] + 1. \tag{4}$$

---

[1] https://github.com/alphapsa/PIPE

Table 1. Logs of CHEOPS observations.

Visit #	Start Date (2021)	End Date (2021)	File Key	Num. of subarrays	Num. of imagettes
1	2021-07-27 11:09:49	2021-07-27 22:09:36	PR100016_TG013701	830	2490
2	2021-08-03 12:11:49	2021-08-03 23:21:58	PR100016_TG013702	861	2583
3	2021-08-06 23:50:49	2021-08-07 11:59:10	PR100016_TG013703	911	2733
4	2021-08-10 12:25:49	2021-08-10 23:35:58	PR100016_TG013704	877	2631
5	2021-08-21 03:09:49	2021-08-21 14:11:55	PR100016_TG013705	901	2703
6	2021-08-31 17:06:49	2021-09-01 04:07:45	PR100016_TG013706	884	2652
7	2021-09-04 04:34:49	2021-09-04 15:44:58	PR100016_TG013707	876	2628
8	2021-09-11 05:45:48	2021-09-11 17:06:55	PR100016_TG013708	886	2658
9	2021-09-18 07:03:59	2021-09-18 18:06:40	PR100016_TG013709	840	2520
10	2021-09-21 20:58:49	2021-09-22 07:47:39	PR100016_TG013710	756	2268

Notes. Time notation follows the ISO-8601 convention. The File Key aids the retrieval of data from the CHEOPS archive.

Table 2. Measured occultation depths.

Visit #	Mid occultation (BJD−2 459 400)	Depth [ppm]	σ [ppm]
1	23.20009	14.8	11.6
2	30.24419	31.9	9.3
3	33.77430	25.2	9.8
4	37.29726	10.3	8.3
5	47.86952	-1.6	10.8
6	58.44554	21.8	10.1
7	61.97386	31.0	9.5
8	69.01787	24.5	9.9
9	76.06736	40.4	10.0
10	79.59218	17.1	13.2

Commensurate with the limited amount of information that is measured, the absorption cross section is assumed to depend only on H_2O and Na,

$$\sigma_{abs} = X_{H_2O}\, \sigma_{H_2O} + X_{Na}\, \sigma_{Na}, \tag{5}$$

where the mixing ratios of H_2O and Na are denoted by X_{H_2O} and X_{Na}, respectively. Other absorbers such as CH_4 or CO are not sufficiently abundant to produce significant opacities in the considered bandpass.

The cross section of H_2O (σ_{H_2O}) was computed using input from the ExoMol spectroscopic line-list database (Polyansky et al. 2018) and using the open-source HELIOS-K opacity calculator[2] (Grimm & Heng 2015; Grimm et al. 2021). It is publicly available in the Swiss-based DACE opacity database[3] (Grimm et al. 2021).

The cross section of Na (σ_{Na}) was computed using Kurucz line-list data (Kurucz & Bell 1995). We accounted for the natural line width, thermal broadening, and pressure broadening using the tabulated van der Waals broadening coefficients from the line list. The latter ones were scaled from collisions with atomic hydrogen to those of collisions with molecular hydrogen by using the Unsöld approximation (Unsöld 1955). The strong resonance lines of Na are known to deviate from the usual Voigt profiles. Their strongly non-Lorentzian far-wing line profiles originating
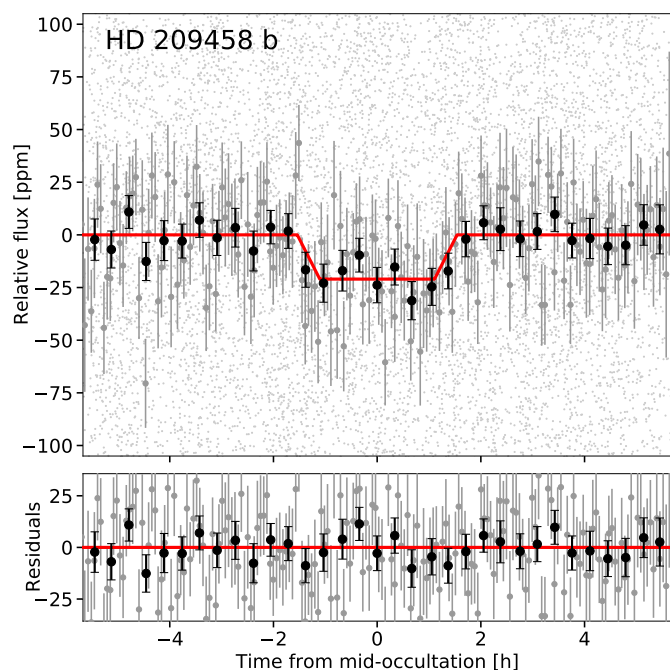
---

[2] https://github.com/exoclime/HELIOS-K
[3] https://dace.unige.ch

Fig. 1. Phase-folded data with best-fit occultation model (unbroken red line). Individual imagette measurements have an average photometric uncertainty of 237 ppm and fill the figure with small, light grey points. To better visualise the occultation, data points are also shown averaged to 3.7 min bins (grey) and 20.5 min bins (black). The bin sizes are chosen to divide the occultation duration into an integer number of bins. The lower panel shows the residuals after the occultation model was subtracted from the data.

from collisions with H_2 were calculated based on Allard et al. (2019).

To compute these cross sections, we assumed a temperature of 1500 K. This is consistent with the brightness temperature measured by Spitzer (Zellem et al. 2014; Evans et al. 2015). We also assumed a pressure of 0.1 bar (Line et al. 2016).

We computed X_{H_2O} using previously benchmarked formulae (Heng & Tsai 2016), assuming the chemical abundance of the Sun (Lodders 2003) scaled to that of the star (close to the solar value at [Fe/H] = 0.04 ± 0.01; Sousa et al. 2021). This yielded the input elemental abundances of carbon, oxygen, and nitrogen: C/H = 2.69×10^{-4}, O/H = 5.37×10^{-4}, and N/H = $7.41 \times$
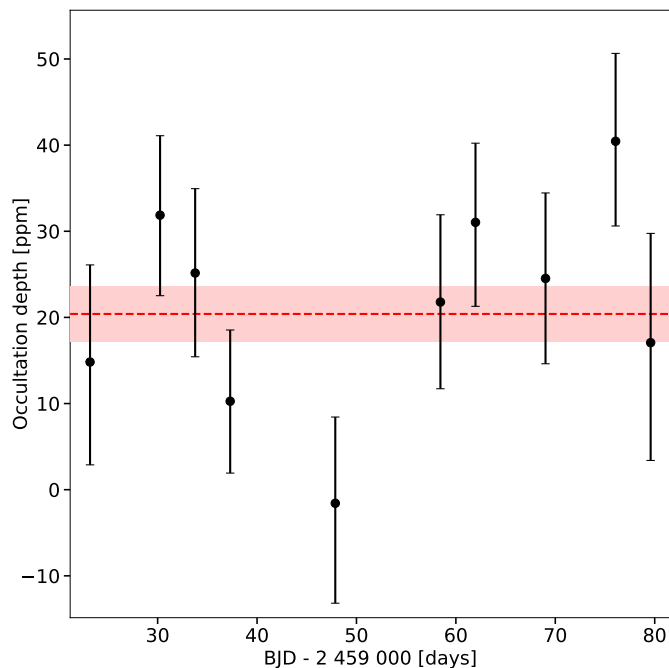
Fig. 2. Occultation measurements from the ten individual visits, plotted against the time of their observation (in barycentric Julian dates, BJD). The dashed red line is the multivisit-fitted depth $20.4^{+3.2}_{-3.3}$ ppm, and the shaded red region shows the 1σ uncertainty region.

10^{-5}. These elemental abundances correspond to C/O = 0.50 and N/O = 0.14. With these inputs, the volume mixing ratio of H_2O is $X_{H_2O} = 5.36 \times 10^{-4}$.

Formally, $A_{g,\lambda}$ is defined at a single wavelength. In practice, the occultation depth is measured across a range of optical/visible wavelengths, which yields a bandpass-integrated geometric albedo,

$$A_g = \frac{\int A_{g,\lambda}\, \lambda\, F_\star\, \mathcal{F}\, d\lambda}{\int \lambda\, F_\star\, \mathcal{F}\, d\lambda}, \qquad (6)$$

where $F_\star$ is the spectral energy distribution of the star, and $\mathcal{F}$ is the bandpass filter. For the HD 209458 star, we obtained $F_\star$ from the *HST* Calibration Database CALSPEC[4] (Bohlin et al. 2014). The bandpass filters for the CHEOPS, MOST, and TESS telescopes were downloaded from the SVO filter service (Rodrigo et al. 2012; Rodrigo & Solano 2020). The factor of λ in the integrands accounts for the conversion of energy into photon flux.

3. Results

From the simultaneous fit to all visits, we find the occultation depth to be $L = 20.4^{+3.2}_{-3.3}$ ppm (Fig. 1). This is consistent with the average over individual fits (Fig. 2, Table 2), $L = 21.4^{+3.3}_{-3.4}$ ppm. Adopting the simultaneous fit and subtracting a 2.2 ppm contribution from thermal emission, we find a geometric albedo $A_g = 0.096 \pm 0.016$.

In the left panel of Fig. 3, we show examples of geometric albedo spectra $A_{g,\lambda}$, derived assuming an atmosphere of the same chemical composition as the star (with $X_{Na} = 2.19 \times 10^{-6}$ and $X_{H_2O} = 5.36 \times 10^{-4}$ from chemical balance). If H_2O is the only

----

[4] The FITS file `hd209458_stisnic_006.fits` available at http://www.stsci.edu/hst/observatory/crds/calspec.html

absorber present, then we obtain a CHEOPS bandpass-integrated geometric albedo of $A_g = 0.41$, which is much higher than the measurement. If Na and H_2O are included, then we obtain $A_g = 0.11$; if only Na is considered, we obtain $A_g = 0.12$. This confirms the prediction of Sudarsky et al. (2000): one reason why hot Jupiters are dark in the optical/visible range of wavelengths is absorption by the resonant doublet of Na (see also Seager & Sasselov 2000).

In theory, the geometric albedo is a monochromatic quantity. In practice, the bandpass-integrated geometric albedo A_g differs when it is measured by the MOST, CHEOPS, and TESS space telescopes because the bandpass filters cover different ranges of wavelengths (left panel of Fig. 3). Our calculations indicate that Na is the dominant absorber in shaping the albedo spectrum across optical/visible wavelengths (Seager & Sasselov 2000; Sudarsky et al. 2000). In the right panel of Fig. 3, we compute A_g for all three bandpasses and allow the relative abundance (by number) of Na to vary. The measured CHEOPS geometric albedo of 0.096 ± 0.016 is consistent with the theoretical geometric albedo derived from a stellar Na abundance. This does not rule out the possibility that other relative abundances of elements may reproduce A_g, but the close match between the measured and predicted A_g from the simplest hypothesis of an atmosphere with the same chemical abundance as the star is remarkable.

4. Conclusions and discussion

The right panel of Fig. 3 demonstrates that the TESS geometric albedo is expected to be $\lesssim 0.03$ for $X_{Na} \sim 10^{-6}$. This translates into an occultation depth of $\lesssim 6$ ppm in the TESS band from purely reflected light. When we add a 8.5 ppm thermal contribution as estimated from the model atmosphere (Sect. 2.1), we obtain a total expected occultation depth of $\lesssim 15$ ppm. This is not detectable by TESS because we estimate that its 3σ detection threshold would be ~ 50 ppm for an observation duration of a single sector (corresponding to $A_g = 0.25$).

As already pointed out by Heng et al. (2021), reflected-light phase curves that are free of clouds are expected to have a distinct shape associated with Rayleigh scattering (Fig. 4). Using Monte Carlo simulations of observations, we find that the noise must be lower than 4.5 ppm per hour of the phase curve in order to distinguish Rayleigh from isotropic scattering with better than 95% confidence. This will be challenging to achieve considering the variability of the star (Rowe et al. 2006, 2008). Fortunately, confusion of the orbital phase with stellar rotation modulation will be mitigated by their very different timescales (the rotation period is about two weeks, as inferred from Casasayas-Barris et al. 2021).

The measured geometric albedo of HD 209458 b is consistent with a cloud-free, stellar-metallicity atmosphere. This corroborates the findings of Sudarsky et al. (2000), who predicted that "Class IV roasters", as they called them, have low geometric albedos due to absorption by alkali metals (see also Seager & Sasselov 2000).

Our result demonstrates the unique capability of CHEOPS to measure the geometric albedo through ultra-high-precision photometry of occultations at optical wavelengths. It is highly desirable to apply this technique to a larger sample to improve our understanding of planetary atmospheres and their energy balance. A publication is in preparation by the CHEOPS consortium to present updated and more detailed performance estimates for various scenarios, derived from experience with the first two years of data.

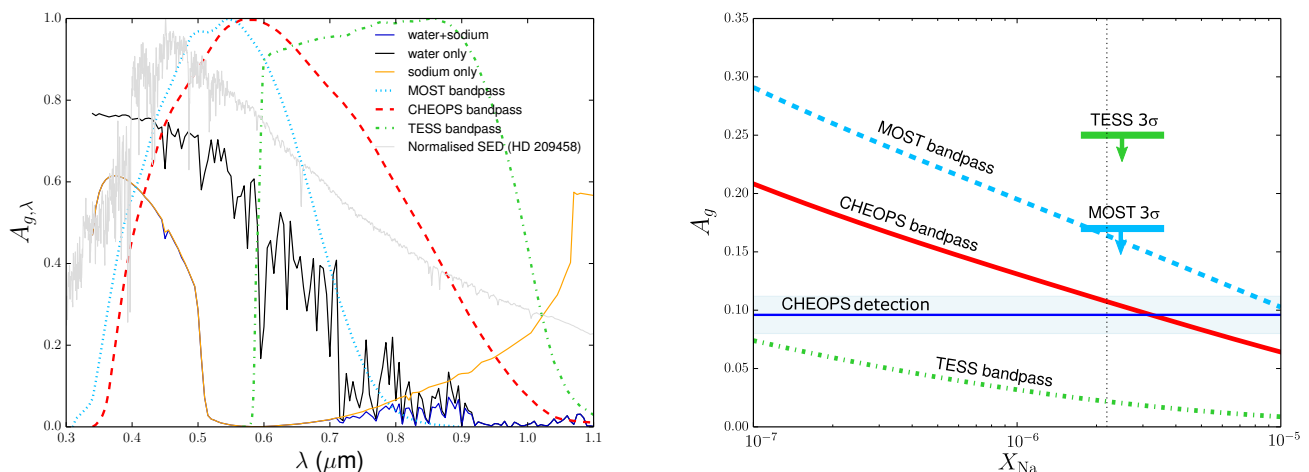**Fig. 3.** Bandpass-dependent geometric albedos. Left panel: Examples of geometric albedo spectra assuming stellar abundances of H_2O ($X_{H_2O} = 5.36 \times 10^{-4}$) and/or Na ($X_{Na} = 2.19 \times 10^{-6}$). The corresponding bandpass-integrated CHEOPS geometric albedos for H_2O and Na, H_2O only, and Na only are $A_g = 0.11$, 0.41, and 0.12, respectively. The bandpass filters of the CHEOPS, MOST, and TESS space telescopes are overlaid, as are the normalised spectral energy distribution of the HD 209458 star (where the fluxes have been divided by their maximum value such that they have no physical units). Right panel: Modelled bandpass-integrated geometric albedos for MOST, CHEOPS, and TESS bandpasses assuming a stellar abundance of H_2O, but with varying volume mixing ratios of Na. The vertical dotted line corresponds to $X_{Na} = 2.19 \times 10^{-6}$, the Na abundance of the star. The horizontal line with the associated shaded region depicts the $A_g = 0.096 \pm 0.016$ measurement reported in this study, and the MOST and predicted TESS 3σ upper limits are added as horizontal lines. All calculations assume a temperature of 1500 K; calculations with 1400 K produce a very similar outcome (not shown).
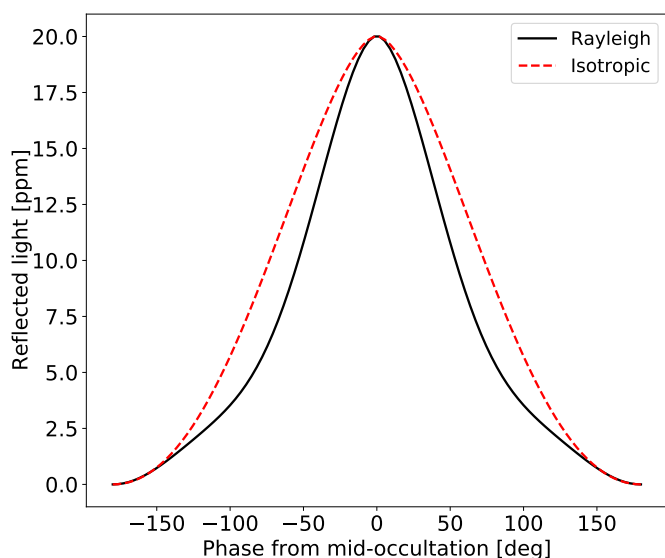
Fig. 4. Predicted reflected light relative to the star as a function of phase for Rayleigh and isotropic scattering in the CHEOPS photometric band from HD 209458 b, computed using the formulation in Heng et al. (2021). The single-scattering albedos ω were 0.45 for Rayleigh scattering and 0.55 for isotropic scattering. While the phase curve itself should be detectable with CHEOPS, it will be challenging to distinguish between the two scattering laws.

References

Albrecht, S., Winn, J. N., Johnson, J. A., et al. 2012, ApJ, 757, 18
Allard, N. F., Spiegelman, F., Leininger, T., & Molliere, P. 2019, A&A, 628, A120
Angerhausen, D., DeLarme, E., & Morse, J. A. 2015, PASP, 127, 1113
Beatty, T. G., Madhusudhan, N., Tsiaras, A., et al. 2017, AJ, 154, 158
Benz, W., Broeg, C., Fortier, A., et al. 2021, Experimental Astronomy, 51, 109
Bohlin, R. C., Gordon, K. D., & Tremblay, P. E. 2014, PASP, 126, 711
Bonomo, A. S., Desidera, S., Benatti, S., et al. 2017, A&A, 602, A107
Boyajian, T., von Braun, K., Feiden, G. A., et al. 2015, MNRAS, 447, 846
Casasayas-Barris, N., Palle, E., Stangret, M., et al. 2021, A&A, 647, A26
Casasayas-Barris, N., Pallé, E., Yan, F., et al. 2020, A&A, 635, A206
Charbonneau, D., Brown, T. M., Latham, D. W., & Mayor, M. 2000, ApJ, 529, L45
Charbonneau, D., Brown, T. M., Noyes, R. W., & Gilliland, R. L. 2002, ApJ, 568, 377
Cox, A. N. 2000, Allen's Astrophysical Quantities (Springer-Verlag)
Crossfield, I. J. M., Knutson, H., Fortney, J., et al. 2012, ApJ, 752, 81
Cubillos, P. E., Fossati, L., Koskinen, T., et al. 2020, AJ, 159, 111
Deming, D., Seager, S., Richardson, L. J., & Harrington, J. 2005, Nature, 434, 740
Demory, B.-O., de Wit, J., Lewis, N., et al. 2013, ApJ, 776, L25
Demory, B.-O., Seager, S., Madhusudhan, N., et al. 2011, ApJ, 735, L12
Esteves, L. J., De Mooij, E. J. W., & Jayawardhana, R. 2015, ApJ, 804, 150
Evans, T. M., Aigrain, S., Gibson, N., et al. 2015, MNRAS, 451, 680
Evans, T. M., Pont, F., Sing, D. K., et al. 2013, ApJ, 772, L16
Gao, P., Thorngren, D. P., Lee, E. K. H., et al. 2020, Nature Astronomy, 4, 951
Grimm, S. L. & Heng, K. 2015, ApJ, 808, 182
Grimm, S. L., Malik, M., Kitzmann, D., et al. 2021, ApJS, 253, 30
Hapke, B. 1981, J. Geophys. Res., 86, 3039
Heng, K. & Demory, B.-O. 2013, ApJ, 777, 100
Heng, K., Morris, B. M., & Kitzmann, D. 2021, Nature Astronomy, 5, 1001
Heng, K. & Tsai, S.-M. 2016, ApJ, 829, 104
Henry, G. W., Marcy, G. W., Butler, R. P., & Vogt, S. S. 2000, ApJ, 529, L41
Hooton, M. J., Hoyer, S., Kitzmann, D., et al. 2021, arXiv e-prints, arXiv:2109.05031
Hoyer, S., Guterman, P., Demangeon, O., et al. 2020, A&A, 635, A24
Hunter, J. D. 2007, Computing in Science & Engineering, 9, 90
Jensen, A. G., Redfield, S., Endl, M., et al. 2011, ApJ, 743, 203
Kipping, D. & Bakos, G. 2011, ApJ, 730, 50
Knutson, H. A., Charbonneau, D., Noyes, R. W., Brown, T. M., & Gilliland, R. L. 2007, ApJ, 655, 564
Kurucz, R. & Bell, B. 1995, Atomic Line Data (R.L. Kurucz and B. Bell) Kurucz CD-ROM No. 23. Cambridge, Mass.: Smithsonian Astrophysical Observatory, 1995., 23
Lecavelier Des Etangs, A., Vidal-Madjar, A., Désert, J. M., & Sing, D. 2008, A&A, 485, 865
Lendl, M., Csizmadia, S., Deline, A., et al. 2020, A&A, 643, A94
Line, M. R., Stevenson, K. B., Bean, J., et al. 2016, AJ, 152, 203
Lodders, K. 2003, ApJ, 591, 1220
Maxted, P. F. L., Ehrenreich, D., Wilson, T. G., et al. 2021, MN-RAS[arXiv:2111.08828]
Mollière, P., van Boekel, R., Dullemond, C., Henning, T., & Mordasini, C. 2015, ApJ, 813, 47
Morris, B. M., Heng, K., Brandeker, A., Swan, A., & Lendl, M. 2021, A&A, 651, L12
Polyansky, O. L., Kyuberis, A. A., Zobov, N. F., et al. 2018, MNRAS, 480, 2597
Rodrigo, C. & Solano, E. 2020, in XIV.0 Scientific Meeting (virtual) of the Spanish Astronomical Society, 182
Rodrigo, C., Solano, E., & Bayo, A. 2012, SVO Filter Profile Service Version 1.0, IVOA Working Draft 15 October 2012
Rowe, J. F., Matthews, J. M., Seager, S., et al. 2006, ApJ, 646, 1241
Rowe, J. F., Matthews, J. M., Seager, S., et al. 2008, ApJ, 689, 1345
Russell, H. N. 1916, ApJ, 43, 173
Santos, N. C., Cristo, E., Demangeon, O., et al. 2020, A&A, 644, A51
Seager, S. 2010, Exoplanet Atmospheres: Physical Processes (Princeton University Press)
Seager, S. & Sasselov, D. D. 2000, ApJ, 537, 916

Shapiro, S. S. & Wilk, M. B. 1965, Biometrika, 52, 591
Sing, D. K., Fortney, J. J., Nikolov, N., et al. 2016, Nature, 529, 59
Sing, D. K., Vidal-Madjar, A., Désert, J. M., Lecavelier des Etangs, A., & Ballester, G. 2008, ApJ, 686, 658
Snellen, I. A. G., Albrecht, S., de Mooij, E. J. W., & Le Poole, R. S. 2008, A&A, 487, 357
Sousa, S. G., Adibekyan, V., Delgado-Mena, E., et al. 2021, A&A, 656, A53
Southworth, J. 2010, MNRAS, 408, 1689
Stassun, K. G., Collins, K. A., & Gaudi, B. S. 2017, AJ, 153, 136
Stevenson, K. B. 2016, ApJ, 817, L16
Sudarsky, D., Burrows, A., & Pinto, P. 2000, ApJ, 538, 885
Swain, M. R., Vasisht, G., Tinetti, G., et al. 2009, ApJ, 690, L114
Szabó, G. M., Gandolfi, D., Brandeker, A., et al. 2021, A&A, 654, A159
Torres, G., Winn, J. N., & Holman, M. J. 2008, ApJ, 677, 1324
Unsöld, A. 1955, Physik der Sternatmosphären, mit besonderer Berücksichtigung der Sonne. (Julius Springer, Berlin)
Vidal-Madjar, A., Désert, J. M., Lecavelier des Etangs, A., et al. 2004, ApJ, 604, L69
Vidal-Madjar, A., Lecavelier des Etangs, A., Désert, J. M., et al. 2003, Nature, 422, 143
Wong, I., Kitzmann, D., Shporer, A., et al. 2021, AJ, 162, 127
Wong, I., Shporer, A., Daylan, T., et al. 2020, AJ, 160, 155
Zellem, R. T., Lewis, N. K., Knutson, H. A., et al. 2014, ApJ, 790, 53

¹ Department of Astronomy, Stockholm University, AlbaNova University Center, 10691 Stockholm, Sweden

² Center for Space and Habitability, Gesellsschaftstrasse 6, 3012 Bern, Switzerland

³ Department of Physics, University of Warwick, Gibbet Hill Road, Coventry CV4 7AL, United Kingdom

⁴ Observatoire Astronomique de l'Université de Genève, Chemin Pegasi 51, Versoix, Switzerland

⁵ Physikalisches Institut, University of Bern, Gesellsschaftstrasse 6, 3012 Bern, Switzerland

⁶ Aix Marseille Univ, CNRS, CNES, LAM, 38 rue Frédéric Joliot-Curie, 13388 Marseille, France

⁷ Division Technique INSU, BP 330, 83507 La Seyne cedex, France

⁸ Astrophysics Group, Keele University, Staffordshire, ST5 5BG, United Kingdom

⁹ Instituto de Astrofisica e Ciencias do Espaco, Universidade do Porto, CAUP, Rua das Estrelas, 4150-762 Porto, Portugal

¹⁰ Departamento de Fisica e Astronomia, Faculdade de Ciencias, Universidade do Porto, Rua do Campo Alegre, 4169-007 Porto, Portugal

¹¹ Astrobiology Research Unit, Université de Liège, Allée du 6 Août 19C, B-4000 Liège, Belgium

¹² Space sciences, Technologies and Astrophysics Research (STAR) Institute, Université de Liège, Allée du 6 Août 19C, 4000 Liège, Belgium

¹³ INAF, Osservatorio Astronomico di Padova, Vicolo dell'Osservatorio 5, 35122 Padova, Italy

¹⁴ Instituto de Astrofisica de Canarias, 38200 La Laguna, Tenerife, Spain

¹⁵ Departamento de Astrofisica, Universidad de La Laguna, 38206 La Laguna, Tenerife, Spain

¹⁶ Institut de Ciencies de l'Espai (ICE, CSIC), Campus UAB, Can Magrans s/n, 08193 Bellaterra, Spain

¹⁷ Institut d'Estudis Espacials de Catalunya (IEEC), 08034 Barcelona, Spain

¹⁸ Admatis, 5. Kandó Kálmán Street, 3534 Miskolc, Hungary

¹⁹ Depto. de Astrofisica, Centro de Astrobiologia (CSIC-INTA), ESAC campus, 28692 Villanueva de la Cañada (Madrid), Spain

²⁰ Space Research Institute, Austrian Academy of Sciences, Schmiedlstrasse 6, A-8042 Graz, Austria

²¹ Université Grenoble Alpes, CNRS, IPAG, 38000 Grenoble, France

²² Institute of Planetary Research, German Aerospace Center (DLR), Rutherfordstrasse 2, 12489 Berlin, Germany

²³ Université de Paris, Institut de physique du globe de Paris, CNRS, F-75005 Paris, France

²⁴ Centre for Exoplanet Science, SUPA School of Physics and Astronomy, University of St Andrews, North Haugh, St Andrews KY16 9SS, UK

²⁵ ESTEC, European Space Agency, 2201AZ, Noordwijk, NL

²⁶ Centre for Mathematical Sciences, Lund University, Box 118, 221 00 Lund, Sweden

²⁷ Leiden Observatory, University of Leiden, PO Box 9513, 2300 RA Leiden, The Netherlands

²⁸ Department of Space, Earth and Environment, Chalmers University of Technology, Onsala Space Observatory, 43992 Onsala, Sweden

²⁹ Dipartimento di Fisica, Universita degli Studi di Torino, via Pietro Giuria 1, I-10125, Torino, Italy

³⁰ University of Vienna, Department of Astrophysics, Türkenschanzstrasse 17, 1180 Vienna, Austria

³¹ Science and Operations Department - Science Division (SCI-SC), Directorate of Science, European Space Agency (ESA), European Space Research and Technology Centre (ESTEC),Keplerlaan 1, 2201-AZ Noordwijk, The Netherlands

³² Konkoly Observatory, Research Centre for Astronomy and Earth Sciences, 1121 Budapest, Konkoly Thege Miklós út 15-17, Hungary

³³ ELTE Eötvös Loránd University, Institute of Physics, Pázmány Péter sétány 1/A, 1117 Budapest, Hungary

³⁴ IMCCE, UMR8028 CNRS, Observatoire de Paris, PSL Univ., Sorbonne Univ., 77 av. Denfert-Rochereau, 75014 Paris, France

³⁵ Institut d'astrophysique de Paris, UMR7095 CNRS, Université Pierre & Marie Curie, 98bis blvd. Arago, 75014 Paris, France

³⁶ Department of Astrophysics, University of Vienna, Tuerkenschanzstrasse 17, 1180 Vienna, Austria

³⁷ INAF, Osservatorio Astrofisico di Catania, Via S. Sofia 78, 95123 Catania, Italy

³⁸ Institute of Optical Sensor Systems, German Aerospace Center (DLR), Rutherfordstrasse 2, 12489 Berlin, Germany

³⁹ Dipartimento di Fisica e Astronomia "Galileo Galilei", Universita degli Studi di Padova, Vicolo dell'Osservatorio 3, 35122 Padova, Italy

⁴⁰ Cavendish Laboratory, JJ Thomson Avenue, Cambridge CB3 0HE, UK

⁴¹ ETH Zürich, Department of Physics, Wolfgang-Pauli-Strasse 27, 8093 Zürich, Switzerland

⁴² Center for Astronomy and Astrophysics, Technical University Berlin, Hardenberstrasse 36, 10623 Berlin, Germany

⁴³ Institut für Geologische Wissenschaften, Freie Universität Berlin, 12249 Berlin, Germany

⁴⁴ ELTE Eötvös Loránd University, Gothard Astrophysical Observatory, 9700 Szombathely, Szent Imre h. u. 112, Hungary

⁴⁵ MTA-ELTE Exoplanet Research Group, 9700 Szombathely, Szent Imre h. u. 112, Hungary

⁴⁶ MTA-ELTE Lendület "Momentum" Milky Way Research Group, Hungary

⁴⁷ Institute of Astronomy, University of Cambridge, Madingley Road, Cambridge, CB3 0HA, United Kingdom

Appendix A: Assumed and derived parameters

Table A.1. Assumed and derived parameters.

Parameters from literature	Symbol	Value	Units	References / Comment
Period	P_0	3.52474859	days	1
Transit time	BJD_0	2 452 826.629283	days	2
Planet-to-star radii ratio	$R_p/R_\star$	0.12175 ± 0.00011	-	3, 4, 5, 6
Normalised semi-major axis	$a/R_\star$	8.807 ± 0.051	-	1, 3, 6, 7
Orbital inclination	i	86.744 ± 0.022	deg	3, 6, 7, 8
Transit depth	D	14822 ± 28	ppm	Calculated from $R_p/R_\star$
Transit duration	T_{14}	0.12840 ± 0.00096	days	Calc. from P_0, $a/R_\star$, i, and $R_p/R_\star$
Fitted parameter priors	**Symbol**	**Prior***	**Units**	**Comment**
Occultation phase width	W	$\mathcal{N}(0.03643, 0.00054)$		$W = T_{14}/P_0$
Occultation depth	L	$\mathcal{U}(1, 200)$	ppm	Except visit 5[†]
Impact parameter	b	$\mathcal{N}(0.5002, 0.0090)$		Calculated from $a/R_\star$ and i
Time of inferior conjunction[‡]	T_0	$\mathcal{N}(T_0, 0.01)$	days	Calculated from P_0 and BJD_0
Fitted parameter posteriors	**Symbol**	**Posterior**	**Units**	**Comment**
Occultation phase width	W	0.0366 ± 0.0003		
Occultation depth	L	20.4 ± 3.3	ppm	
Impact parameter	b	0.5000 ± 0.007		
Time of inferior conjunction[‡]	T_0	0.156 ± 0.003	days	Add 2 459 453 for BJD

Notes. The table shows parameters fixed from the literature and parameters fit using priors, with their posteriors. For the parameters with multiple references, we computed a weighted average. References: (1) Stassun et al. (2017), (2) Bonomo et al. (2017), (3) Evans et al. (2015), (4) Boyajian et al. (2015), (5) Albrecht et al. (2012), (6) Torres et al. (2008), (7) Southworth (2010), (8) Knutson et al. (2007). [*] $\mathcal{N}$ and $\mathcal{U}$ denote normal and uniform distributions, respectively. [†] For visit 5, the occultation depth was derived with an unconstraining prior $\mathcal{U}(-\infty, \infty)$ because the MCMC analysis did not converge with the constrained one. [‡] Also called mid-transit epoch.
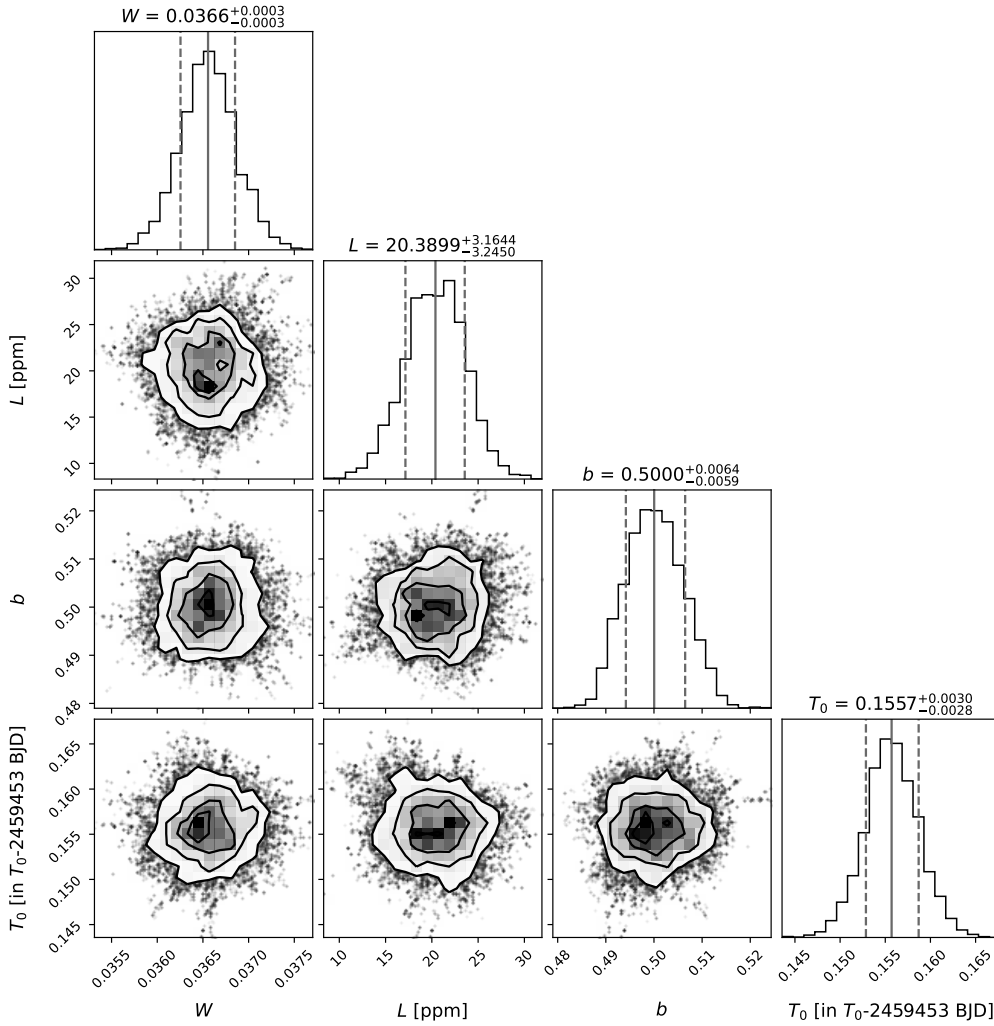
Fig. A.1. Correlation plots for the fitted parameters.